

# The Spectrum of SS 433 in the *H* and *K* Bands

Edward L. Robinson<sup>1</sup>, Cynthia S. Froning<sup>1</sup>, Daniel T. Jaffe<sup>1</sup>, Kyle F. Kaplan<sup>1</sup>, Hwi Hyun Kim<sup>1,2</sup>, Gregory N. Mace<sup>1</sup>, Kimberly R. Sokal<sup>1</sup>,

and

Jae-Joon Lee<sup>2</sup>

Received \_\_\_\_\_; accepted \_\_\_\_\_

arXiv:1704.08166v1 [astro-ph.SR] 26 Apr 2017

---

<sup>1</sup>Department of Astronomy, University of Texas at Austin, C1400, Austin, TX 78712;  
elr@astro.as.utexas.edu

<sup>2</sup>Korea Astronomy and Space Science Institute, 776 Daeduk-daero, Yuseong-gu, Daejeon  
305-348, Republic of Korea

## ABSTRACT

SS 433 is an X-ray binary and the source of sub-relativistic, precessing, baryonic jets. We present high-resolution spectrograms of SS 433 in the infrared  $H$  and  $K$  bands. The spectrum is dominated by hydrogen and helium emission lines. The precession phase of the emission lines from the jet continues to be described by a constant period,  $P_{jet} = 162.375$  d. The limit on any secularly changing period is  $|\dot{P}| \lesssim 10^{-5}$ . The He I  $\lambda 2.0587 \mu\text{m}$  line has complex and variable P-Cygni absorption features produced by an inhomogeneous wind with a maximum outflow velocity near  $900 \text{ km s}^{-1}$ . The He II emission lines in the spectrum also arise in this wind. The higher members of the hydrogen Brackett lines show a double-peaked profile with symmetric wings extending more than  $\pm 1500 \text{ km s}^{-1}$  from the line center. The lines display radial velocity variations in phase with the radial velocity variation expected of the compact star, and they show a distortion during disk eclipse that we interpret as a rotational distortion. We fit the line profiles with a model in which the emission comes from the surface of a symmetric, Keplerian accretion disk around the compact object. The outer edge of the disk has velocities that vary from  $110$  to  $190 \text{ km s}^{-1}$ . These comparatively low velocities place an important constraint on the mass of the compact star: Its mass must be less than  $2.2 M_{\odot}$  and is probably less than  $1.6 M_{\odot}$ .

*Subject headings:* binaries: close — infrared: stars — stars: individual (SS 433) — stars: variables: other

## 1. Introduction

SS 433 is an eclipsing X-ray binary star with an orbital period  $P_{orb} = 13.08223 \pm 0.0007$  days (Brinkmann et al. 2005; Marshall et al. 2013; Goranskii 2011). One component of the binary is an A-type supergiant star and the other must be a neutron star or black hole accreting mass transferred from the A-type star (Brinkmann et al. 1989; Gies et al. 2002b; Barnes et al. 2006; Clark et al. 2007; Hillwig & Gies 2008; Kubota et al. 2010). The system’s main claim to fame is its sub-relativistic ( $V_{jet} \approx 0.26c$ ) baryonic jets (for a broad review of the SS 433 jets see Fabrika (2004)). The jets originally revealed themselves as two systems of hydrogen and helium emission lines, each system Doppler-shifted to the red or blue by up to hundreds of Ångstroms (Margon et al. 1979a; Liebert et al. 1979). Further observations showed that the Doppler shifts of the two systems varied oppositely and symmetrically about redshift  $z \approx 0.04$  in a roughly sinusoidal pattern with a period near 164 days (Margon et al. 1979b). Milgrom (1979a) and Fabian & Rees (1979) proposed that the two systems were produced by narrowly-columnated, oppositely-directed, precessing jets. A simple kinematic model based on this physical model is a good descriptor of the observed jet redshifts (Abell & Margon 1979; Margon 1984). High resolution radio maps of SS 433 are in accord with the optically-derived model (Roberts et al. 2008; Bell et al. 2011). An update to the kinematic model by Eikenberry et al. (2001) yielded precise values for the orbital inclination  $i = 78.05^\circ \pm 0.05^\circ$ , the angle between the jet and the precession axis  $\theta = 20.92^\circ \pm 0.08^\circ$ , the precession period  $P_{jet} = 162.375 \pm 0.011$  days, and the jet speed  $\beta = V_{jet}/c = 0.2647 \pm 0.0008$  or  $\Gamma = (1 - \beta^2)^{-1/2} = 1.037$ . The kinematic model only agrees with the observed jet properties in the mean, though. The jets “nod” at a period of 6.3 days, which is the beat period between  $P_{jet}$  and  $P_{orb}/2$  (Katz et al. 1982); the jets are a series of clumps or “bullets”, not a continuous stream (Murden et al. 1980; Vermeulen et al. 1993); and there is intrinsic jitter in both precession phase and jet velocity (Eikenberry et al. 2001). The jet velocity has been attributed to line-locking in hydrogenic

ions (Milgrom 1979b; Shapiro et al. 1986). Taken together, the line locking mechanism and the strong H and He emission lines demonstrate that the jets are dominated by baryons.

While the basic properties of the jets in SS 433 are well established, the same cannot be said about most of the other properties of SS 433. The existence of the jets implies the presence of a precessing accretion disk around the compact star. There is abundant indirect evidence for the disk, but direct evidence for it is meager. The primary eclipses in the optical light curve can be understood as eclipses of an accretion disk that precesses with, and is perpendicular to the jets (Goranskii et al. 1998; Cherepashchuk 2002). The non-jet emission lines are generally called stationary lines (stationary only by comparison!). Perez & Blundell (2009, 2010) fitted the profiles of the stationary  $H\alpha$ ,  $H\beta$ , and  $Br\gamma$  emission line with 4 to 6 Gaussians for each line. Two of the Gaussians were consistently displaced by  $\pm(500 - 600)$  km s<sup>-1</sup> from the line centers. They associated these components with the accretion disk. Filippenko et al. (1988) successfully modeled the broad, double-peaked profiles of the stationary emission lines in the higher members of the Paschen series with theoretical accretion disk line profiles, although Fabrika (2004) preferred to attribute the profiles to disk winds and other gas outflows.

A disk wind is certainly present (Fabrika 2004). The stationary Balmer lines are dominated by emission from this wind, not the disk itself, because they are produced in a volume large compared to the orbit of the binary star and because the radial velocity variations of the lines are not in phase with the radial velocity variations expected for gas around the compact star (Murden et al. 1980; Gies et al. 2002a). The wind also reveals itself in  $H\beta$ , He I  $\lambda 5015$ , and sometimes other lines. The wind speeds measured from the absorption components of the P-Cygni profiles range from  $\sim 150$  to  $\sim 1300$  km s<sup>-1</sup>, increasing monotonically as the disk becomes more face on (Fabrika 1997). The maximum wind velocities inferred from models of these absorption features and of the broad wings of

the He II emission lines imply that the maximum wind speed could be several times higher than  $1300 \text{ km s}^{-1}$  (Fabrika 2004; Medvedev et al. 2013). The measured mass loss rates in the wind generally cluster near  $10^{-4} M_{\odot} \text{ yr}^{-1}$  (but see Kotani et al. (1996)). The rate is less certain than the agreement among the measurements might suggest, though, because it depends on *inter alia* the adopted wind speed, the wind geometry, the clumpiness of the wind, and the mass of the compact star (Shklovskii 1981; Blundell et al. 2001; Fuchs et al. 2002; Perez & Blundell 2009). Nevertheless, the mass loss rate is high and connotes an accretion disk around the compact star that is supercritical and vertically extended, at least near the compact star (Fabrika 2004).

The gas outflow is enhanced in the plane of the disk. The enhanced outflow is detected from absorption lines with radial velocities near  $-100 \text{ km s}^{-1}$  that are strongest when the accretion disk is approximately edge-on (Crampton & Hutchings 1981; Fabrika 1997; Fabrika et al. 1997). This outflow is a likely source of some of the absorption seen at X-ray wavelengths (Kotani et al. 1996). Since the amount of absorption depends on the jet precession phase, Kotani et al. (1996) invoked circumbinary material in a precessing plane fed by gas “sprinkled” from the accretion disk. The geometry of the equatorial outflow is uncertain. Fabrika (1997, 2004) pictures the material as a cometary tail coming from the A-type star. Or it may be an expanding spiral wave, perhaps extruded from the outer Lagrangian point or ejected by a propeller, or perhaps produced by a density wake in the stellar wind (Sawada et al. 1986; Welsh et al. 1998; Kim 2011). The outflowing material in the equatorial plane is the likely source of the equatorial “ruff” observed at radio wavelengths (Doolin & Blundell 2009). In any case, there are good observational and theoretical reasons to conclude that the circumbinary material is not confined to circular Keplerian orbits, and that the gas flow is affected by more than simple gravitational dynamics.

There is no agreement on the masses of the two stars, nor even whether the compact star is a neutron star or a black hole. None of the properties that might uniquely identify a neutron star such as type I bursts or periodic flux modulations have been observed (Strohmayer & Bildsten 2006; van der Klis 2006), although quasi-periodic X-ray oscillations with a frequency near 0.1 Hz have been seen (Kotani et al. 2006). Recent measurements of the mass of the compact star range from  $M_X = 1.45 \pm 0.20 M_\odot$  (Goranskii 2011, 2013) to  $M_X \approx 16 M_\odot$  (Gies et al. 2002b; Blundell et al. 2008), and the measurements are not converging (see Kubota et al. (2010) and Goranskii (2011) for reviews of the mass measurements). The higher masses would imply that the compact star is a black hole, but the lower masses would allow it to be a neutron star.

These properties together make SS 433 unlike any other object that has been found in the Galaxy. While it is often included among the microquasars because of the properties of its radio jets (Mirabel & Rodríguez 1999), the underlying system is quite different from the other microquasars, most of which are low-mass and intermediate-mass X-ray binaries. Only recently has a sibling to SS 433 been found, but in another galaxy. M81 ULS-1, an ultraluminous supersoft X-ray source in M81, has moving emission features reminiscent of the jet lines in SS 433 (Liu et al. 2015).

We report here observations of the infrared spectrum of SS 433 in the  $H$  and  $K$  bands at high spectral resolution,  $R = \lambda/\Delta\lambda \approx 45,000$ , and high signal-to-noise ratio (S/N). The previous literature on the infrared spectrum of SS 433 is sparse. Thompson et al. (1979) observed SS 433 in the  $H$  and  $K$  bands at a resolution near  $R \approx 2500$  and with a maximum S/N of  $\sim 10$ . They detected the  $P\alpha$  jet line and stationary emission lines of He I and the hydrogen Brackett series. McAlary & McLaren (1980) and Fuchs et al. (2002) obtained spectrophotometry of SS 433 from 2.0 to 12  $\mu\text{m}$  with good S/N but  $R \lesssim 100$ . Perez & Blundell (2009) observed SS 433 on 14 nights, mostly in the  $K$  band at a resolution

of  $\sim 3900$  and with  $S/N \approx 400$  at  $Br\gamma$ , but published only the  $Br\gamma$  data. Section 2 of our paper describes the observations and Section 3 gives the line identifications for both the jet and the stationary lines. Section 4 discusses the disk model for the higher members of the Brackett lines. Section 5 summarizes and discusses our results.

## 2. Observations and Data Reduction

The Immersion GRating INfrared Spectrograph (IGRINS) measures infrared spectra simultaneously in the  $H$ - and  $K$ -bands ( $1.46$ - $1.81 \mu\text{m}$  and  $1.93$ - $2.47 \mu\text{m}$ ) at a resolving power of  $R \simeq 45,000$  (Park et al. 2014). We observed SS 433 five times between 2014 May and 2015 July with IGRINS on the 2.7-m Harlan J. Smith Telescope at McDonald Observatory. The times of the observations are listed in Table 1. Most observations were obtained in an “ABBA” observing sequence with 300 s exposure times for each individual exposure giving a total of 20 minutes on target. The exceptions are the 2014 May 24 observations, which were obtained in two “AB” sequences of 480 s each for a total of 32 minutes. A nearby A0 star was observed regularly to provide telluric correction, and calibrations (dark, flat field, and Th-Ar arc lamp exposures) were obtained nightly.

The data were reduced using a dedicated Python-based IGRINS data reduction package (Lee 2015).<sup>1</sup> The pipeline performs image calibration, spectrogram extraction, and wavelength calibration. We edited the comparison star spectrograms to flatten the intrinsic absorption features of the A star, and then divided the SS 433 spectrograms by the A star spectrograms to remove telluric absorption and correct for the blaze profile of the spectral orders. We eliminated wavelengths where the signal-to-noise ratio of the A star spectrogram was  $< 20$  and/or the signal in the normalized SS 433 spectrogram dropped below 0.05.

---

<sup>1</sup>see also <https://github.com/igrins/plp>.

Finally, we rebinned the spectrograms to a linear dispersion ( $0.00003 \mu\text{m}/\text{pixel}$  or roughly 1 resolution element) and combined the orders using weighted averages.

There are two primary periodicities in SS 433: the orbital period and the jet precession period. We calculated the orbital phases at which our data were obtained using the orbital ephemeris determined by Goranskii (2011) from data obtained between 1978 and 2007. In this ephemeris  $\phi_{orb} = 0$  corresponds to the time of minimum of the deeper of the two optical eclipses. The orbital phases are listed in Table 1. When extrapolated forward to the epochs of our observations, the formal error on  $\phi_{orb}$  is small,  $\pm 0.004$ , but the eclipsed object is a shape-shifting and aspect-shifting accretion disk, so observed times of minima scatter by more than  $\pm 0.2$  d ( $\Delta\phi_{orb} = \pm 0.015$ ) about the calculated times. More significantly, as shown in Figure 4 in Goranskii (2011), the mean times of eclipse in the RXTE ASM data occur systematically  $\sim 0.027$  in phase after the mean times of eclipse in the optical data. If the X-ray emission arises close to the compact star, this suggests that true orbital conjunction of the stars occurs at orbital phase  $\Delta\phi_{orb} \approx 0.027 \pm 0.004$  after the time of eclipse given by the Goranskij ephemeris. This seemingly small difference between the times of true conjunction and eclipse will become important when we discuss the profiles of the Brackett lines.

To calculate the expected phases and redshifts of the jet lines we used the jet ephemeris from Fabrika (2004). This is the same as the jet ephemeris determined by Eikenberry et al. (2001) except that phase zero is shifted to the times when the jet points most directly at the Earth (when the  $\text{H}\alpha$ – line reaches maximum blueshift), which are also the times when the positive and negative jet lines are most separated in wavelength. We denoted the phase calculated from the Fabrika (2004) version of the ephemeris by  $\Psi_3$  (see Figure 4 in Fabrika (2004) and Figure 1 in Goranskii (2011)). The jet phases at the times of our observations are also listed in Table 1.

### 3. Line Identifications

#### 3.1. The Stationary Lines

Figure 1 shows the infrared spectrum of SS 433 on 2015 May 27 when the jet lines were weak, allowing the stationary emission features to be identified without confusion. The spectrum shows lines in the hydrogen Brackett series and Pfund series, neutral and ionized helium, and the magnesium doublet at  $\lambda\lambda 2.137 - 2.144 \mu\text{m}$  (see Table 2). Fe II lines are often observed in the infrared spectra of early-type emission-line stars, but are absent or too weak to be detected in the spectrum of SS 433 (Chojnowski et al. 2015). Nor do we detect the Na I doublet at  $\lambda\lambda 2.206-2.209 \mu\text{m}$  or any forbidden lines.

The He I  $\lambda 2.0587 \mu\text{m}$  emission line, which arises from the metastable  $2s^1S$  state, shows variable P-Cygni absorption features, the unambiguous signature of wind outflow. The lower panel of Figure 2 shows the He I line on 2014 May 24 and 2015 July 30. The horizontal axis in the figure has been converted to velocity shift with respect to the line’s rest wavelength. The P-Cygni absorption features are variable and complex, showing that the wind is highly inhomogeneous. Individual components of the wind outflow can have velocities up to  $\sim 900 \text{ km s}^{-1}$ . These results agree qualitatively with earlier measurements based on absorption lines. Fabrika (1997), for example, deduced wind speeds between 200 and  $1300 \text{ km s}^{-1}$  (see Figure 18 in Fabrika (2004)). In addition, Figure 5 in Gies et al. (2002a) suggests wind speeds between  $\sim 200$  and  $\sim 600 \text{ km s}^{-1}$  from the P-Cygni absorption in the He I  $\lambda 5876 \text{ \AA}$  line. We do not, though, see the strong dependence of wind speed and absorption line strength on the disk inclination reported by Fabrika (1997). The disk was nearly edge-on on 2015 July 30 and nearly face-on on 2014 May 24 (see Table 4), but the line strengths differed by only a factor of two and the maximum wind speeds differed by just  $\sim 200 \text{ km s}^{-1}$ .

The emission feature near  $\lambda 1.6898 \mu\text{m}$  was an interesting puzzle. An emission feature at a similar wavelength is present in the spectra of many early-type emission-line stars and is usually identified as C I  $\lambda 1.6895 \mu\text{m}$  (Chojnowski et al. 2015). Medvedev et al. (2013) and Goranskii (2011) have shown that the wind should and does produce He II emission lines. Prompted by their work, we instead identify the feature in SS 433 as Doppler-shifted He II  $\lambda 1.6923 \mu\text{m}$  arising in the high-velocity wind. To justify this identification, we note that

- The C I line in the spectra of Be stars is almost always weaker than Fe II  $\lambda 1.6878 \mu\text{m}$ , usually much weaker (see, eg, Figure 5 in Chojnowski et al. (2015)). Neither that Fe II line nor, for that matter, any other Fe II lines are visible in the IGRINS spectrograms of SS 433. Thus, if identified as C I, the feature at  $\lambda 1.6898 \mu\text{m}$  would be anomalously strong relative to other metal lines.
- Although emission lines from carbon are seen in the optical spectrum of SS 433, they are always lines of ionized carbon (eg, C II  $\lambda 7231/7236 \text{ \AA}$  and the C III blend near  $\lambda 4650 \text{ \AA}$ ), not neutral carbon (Liebert et al. 1979; Gies et al. 2002a,b; Schmidtbreick & Blundell 2006; Medvedev et al. 2013).
- If identified as He II, the feature has the wavelength and profile expected for emission from the wind. The top panel of Figure 2 shows the profiles of the feature in the same spectrograms as the He I lines in the bottom panel of the figure. The horizontal axis in the top panel is again the velocity shift with respect to the rest wavelength of the He II  $\lambda 1.6923 \mu\text{m}$  line. The  $\lambda 1.6898 \mu\text{m}$  emission feature lies on the steeply-sloping red wing of the strong Br11 line so its profile is distorted. Emission lines from the wind come from a different volume of the wind than that which causes the P-Cygni absorption. Recognizing that the profiles of emission and absorption lines from an inhomogeneous wind will not, therefore, mimic each other precisely, we see that the

$\lambda 1.6898 \mu\text{m}$  emission feature aligns well with the P-Cygni absorption feature.

- The  $\lambda 1.6923 \mu\text{m}$  line is produced by the 12-7 transition of He II. The He II at  $\lambda 2.1891 \mu\text{m}$  is produced by the 10-7 transition. If our identification is correct, the  $\lambda 2.1891 \mu\text{m}$  line must also be present and should be stronger than the  $\lambda 1.6923 \mu\text{m}$  line. Reference to Figure 1 shows that the  $\lambda 2.1891 \mu\text{m}$  line transition is, indeed, present and that it, too, is distorted and shifted, although not by as much as the  $\lambda 1.6923 \mu\text{m}$  line.

Our identification of the  $\lambda 1.6898 \mu\text{m}$  has important implications. Since the red wing of the line is weaker than the blue wing, something, presumably the accretion disk, is obscuring the wind outflow at positive velocities. Also, since the He II emission comes from an inhomogeneous, variable, partially obscured wind, it is dangerous to use the velocity of the He II lines as a proxy for the orbital radial velocity variations of the compact star.

The only absorption features other than the P-Cygni absorption that we could identify with certainty are two diffuse interstellar absorption bands (DIBs) at  $1.5273$  and  $1.5673 \mu\text{m}$  (Geballe et al. 2011). The DIB at  $1.5273 \mu\text{m}$  is shown in Figure 3, where it shows up as an absorption feature in the Br19 line that is not present in the Br18 or Br20 lines.

### 3.2. The Jet Lines

Figure 4 shows the infrared spectrum of SS 433 on 2014 May 24 when the jet lines were strong. All the jet lines we identified in this and the other four spectrograms are listed in Table 2, and come from neutral hydrogen and helium. The list includes lines that are not normally in the IGRINS bandpasses but can move into the bandpasses when the jet Doppler shifts are large. We see one likely case of bullets in the jets: The  $\text{P}\alpha-$  line on 2014 May 24 (Figure 4) has three peaks that we interpret as coming from three different jet

bullets. The half-width at half maximum of the  $P\alpha$  jet line falls in the range 1000-2000 km  $s^{-1}$ , varying considerably from observation to observation. Although wide in an absolute sense, the jet lines are narrow compared to the total range of projected jet velocities over the 162-day precession period. According to Vermeulen et al. (1993), the jet bullets are typically separated by intervals of  $< 1$  day, so the jet lines usually include emission from more than one bullet. As noted by Vermeulen et al. (1993), the narrowness of the jet lines then means the individual bullets in the jet must cease producing line emission within a day or so after being ejected, traveling just  $\sim 10^{15}$  cm or a few hundred AU before fading.

The mean observed redshifts of the jet lines are given in Table 3 along with the values of  $\Psi_3$  calculated from the Fabrika (2004) ephemeris. The observed redshifts correspond to the peaks of the jet lines. The peaks are often difficult to identify for individual lines, as in the case of the  $P\alpha\pm$  lines in Figure 4, but the mean redshifts are accurate to better than  $\pm 0.001$ . Figure 5 is a plot of the observed redshifts along with the redshift curves predicted by this ephemeris. Shifting the predicted redshift curves by  $\Delta\Psi_3 \approx -0.03$  or about 5 days would be enough to bring them into agreement with the observed redshifts. Since jet nodding and intrinsic phase jitter can introduce phase residuals of 5 to 10 days (Eikenberry et al. 2001), and since we have only five epochs, this small shift could have been introduced by statistical fluctuations. The most we can conclude is that the Eikenberry et al. (2001)/Fabrika (2004) ephemeris predicts of the phase of the jet redshifts to  $|\Delta\Psi_3| \lesssim 0.03$ .

The line identifications listed in Table 2 account for all the strong emission features in the IGRINS spectrograms of SS 433 except for a feature near  $1.966 \mu\text{m}$  that appeared on 2014 May 24 and 2015 July 30 but not in our other spectrograms (marked with a “?” in Figure 4). Although in a region with much telluric absorption, the feature is strong and likely to be real.

## 4. A Disk Model for the Stationary Hydrogen Brackett Lines

### 4.1. Previous Models for the Hydrogen Line Profiles

Most discussions of the stationary hydrogen emission lines have relied almost exclusively on observations of  $H\alpha$ . The line is formed primarily in the disk wind and the wind emission is so strong that it tends to drown out emission from other sources. There are occasional double peaks near the center of  $H\alpha$  that Blundell et al. (2008) and Bowler (2011, 2013) attributed to a rotating disk. Because they did not detect orbital radial velocity variations in the double peaks, Blundell et al. (2008) concluded that the disk is a circumbinary disk or ring. Bowler (2010) suggested that  $H\alpha$  emission from an inner accretion disk around the compact object became visible only during a flare in early 2004 November.

The Paschen and Brackett lines appear to be less dominated by the wind emission, allowing emission from other parts of the SS 433 system to be more visible. Perez & Blundell (2009) fitted  $Br\gamma$  with six Gaussian distributions, which they attributed variously to a multicomponent wind, an inner accretion disk, and an outer accretion disk. The model fits the line profile well, but its functional form is not based on a physical model and it has at least 19 parameters (three for each Gaussian and one for the continuum), so its uniqueness is an issue. Filippenko et al. (1988) observed the higher members of the Paschen series. The lines varied rapidly but on average were double-peaked with broad wings. Filippenko et al. (1988) modeled the mean line profiles with emission from a single, Keplerian accretion disk around the compact star. While the fits were not perfect, the model is physically based, testable, and requires only 6 parameters.

## 4.2. A Disk Model for the Brackett Lines

Like the Paschen lines, the Brackett lines are usually double-peaked and have broad wings. We take, therefore, the same approach as Filippenko et al. (1988) and attempt to fit the Brackett lines with an accretion disk line profile. Our line model is essentially the same as that discussed by Stover (1981) and Smak (1981). The model disk is thin, circular, and in Keplerian motion around the compact star. We assume the line emission comes from an optically and physically thin layer sitting on top of an optically thick disk. The distribution of line emission across the disk is axially symmetric and its radial dependence is given by a power law  $F \propto r^{-\alpha}$ . The local line emission is Doppler broadened by isotropic “turbulent” velocities, which we describe by a Gaussian distribution with a standard deviation  $\sigma = V_{turb}/V_{circ}$ , where  $V_{circ}$  is the local circular velocity. Finally, the emitting layer has a ratio of outer radius to inner radius  $R_{max}/R_{min}$ . These are the inner and outer boundaries of the region producing the line emission, not necessarily the physical boundaries of the disk. Thus the model line profile has three parameters:  $\alpha$ ,  $V_{turb}/V_{circ}$ , and  $R_{max}/R_{min}$ .

Figure 6 shows how the model line profile varies as these three parameters are varied. The basic morphology of the profile – double-peaked with broad wings – is independent of the parameters over their ranges of interest. The dominant effect of varying  $R_{max}/R_{min}$  is to change the separation of the peaks relative to the total line width. The dominant effect of changing  $V_{turb}/V_{circ}$  is to change the depth of the minimum between the two peaks. The dominant effect of changing  $\alpha$  is to change the relative amount of flux in the wings. Another four parameters are needed to fit the model line profiles to the observed line: the continuum level, the line strength, the wavelength of the line center, and a scale parameter for the line width that also absorbs the effect of disk inclination. Thus our model has a total of seven parameters (turbulent broadening adds one parameter to the Filippenko et al. (1988)

model).

The observed line profiles are affected by physical processes not included in our model such as absorption, wind emission, and patchiness in the distribution of the emission whatever its source. These effects systematically distort the observed line profiles, vitiating any attempt to fit the profiles by, say, least squares. Instead, we fitted the profiles by eye, emphasizing the fits to the line wings. This approach precluded a formal error analysis.

### 4.3. Results

In part because Br $\gamma$  is contaminated by jet emission or noise in all but two of our observations, but also because we suspect the higher member of the Brackett series are less contaminated by the wind emission seen in Br $\gamma$  by Perez & Blundell (2009) and are more likely to give a cleaner view of the accretion disk, we modeled only the higher members of the series. Figure 7 shows Br12 and Br13 from all our observations. The Br12 and Br13 profiles agree well with each other, so we fit just the Br12 line, taking it as a proxy for all the higher members of the Brackett series. The fits of the model profiles to the Br12 line are shown in Figures 8 and 9, and the fitted model parameters are listed in Table 4. The table also gives the disk inclination, where we assume the disk is perpendicular to the jet and have calculated the jet inclination from the Eikenberry et al. (2001) jet model.

We do not attach much significance to the fitted values of  $R_{max}/R_{min}$  and  $V_{turb}/V_{circ}$ . While the fitted values of  $R_{max}/R_{min}$  are all near  $R_{max}/R_{min} = 100$ , the values depend sensitively on the placement of the continuum, on noise, and on systematic distortions in the extreme wings of the line. The large values of the ratio mean only that the emission comes from most of the disk, not a narrow ring in the disk. The values of  $V_{turb}/V_{circ}$  all cluster tightly near  $V_{turb}/V_{circ} = 0.20$ , but these values should also be viewed with skepticism. The

only mechanism available to the model for filling the dip between the peaks of the line is turbulent velocity. Many other physical processes could do the same. The rather high value of  $V_{turb}/V_{circ}$  means only that some mechanism is producing low velocity emission that tends to fill the dip.

The fitted values of  $\alpha$ , which are dominated by the fits to the wings of the lines, are more meaningful. Except for the profile on 2014 November 21 (Figure 9), which is contaminated by a jet line, the disk model fits the wings of the observed profiles well. The fitted values of  $\alpha$  differ from observation to observation and these differences correspond to real differences among the observed profiles. This can be seen by comparing the rapidly dropping wings of the profile on 2015 May 27, which yielded  $\alpha = 1.4$ , to the slowly dropping wings of the profile on 2014 May 24, which yielded  $\alpha = 2.1$ . All the values lie in the relatively narrow range  $1.4 \leq \alpha \leq 2.2$ , bracketing the best-fit value  $\alpha = 1.5$  found by Filippenko et al. (1988). This range agrees with the range of values for  $\alpha$  that have been measured from the hydrogen emission lines produced by the accretion disks in cataclysmic variables and low-mass X-ray binaries (Stover 1981; Smak 1981; Johnston et al. 1989; Horne & Saar 1991). Like SS 433, a single cataclysmic variable can also have different values of  $\alpha$  on different nights. Thus, the value of  $\alpha$  ranges from 1.7 to 2.25 in the dwarf nova Z Cha (Horne & Saar 1991).

Although the disk model predicts that double peaks near the line center should always be present, the peaks can be distorted or missing altogether from the observed profiles of the Brackett lines. Both peaks are missing from the Br12 profile on 2015 July 30 (Figure 8). We attribute this to absorption by the accretion disk. On that date the inclination of the disk was  $98^\circ$ , so the disk was nearly edge-on to the Earth. If, as is widely suspected, the disk is vertically extended (Fabrika 2004), the rim of the disk would hide much of the emitting surface layer of the disk. We expect our disk model to fail under these conditions,

especially at the low velocities where the hydrogen lines would be prone to self absorption.

The profiles of the Brackett lines on 2014 November 21 (Figure 9) were single peaked – the blue peak of the line was missing. The orbital phase predicted by the Goranskii (2011) ephemeris for this observation is  $0.004 \pm 0.004$ . Perez & Blundell (2009) have published a montage of Br $\gamma$  line profiles. One of them was obtained at a similar orbital phase ( $\phi_{orb} = 0.96$ ) and was almost identical to the profile we observed. Following the discussion in Section 2, the orbital phase of our observation probably corresponds to a phase  $-0.023$  before true conjunction of the stars. Thus, our observation and the observation by Perez & Blundell (2009) were both made during eclipse but prior to mid-eclipse. At this phase the accretion disk is partly eclipsed and the eclipse would systematically block off parts of the disk with low velocity gas approaching the Earth. The profile would be missing the blue-shifted peak. The line profile can therefore be interpreted as a classical rotational disturbance similar to the rotational disturbance observed in the He II  $\lambda 4686$  Å line from the accretion disk in the old nova DQ Her (Greenstein & Kraft 1959; Kraft 1959).

The separation of the peaks is approximately equal to twice the projected orbital velocity at the outer edge of the disk. We define the deprojected velocity at the outer edge to be 1/2 the velocity separation of the peaks divided by the sine of the disk inclination. The deprojected velocities are listed in the penultimate column of Table 4 and have a mean value of  $148 \text{ km s}^{-1}$ . The velocities on the individual observations range from  $107$  to  $191 \text{ km s}^{-1}$ , and inspection of Figure 8 shows that these differences correspond to large, real differences in the peak separations from profile to profile. In fact, these deprojected velocities may be too low because broadening of the lines by turbulence moves the double peaks towards each other with respect to the line wings. For  $V_{turb}/V_{circ} = 0.20$  this effect reduces the separation of the peaks by about 15%. Correcting for this effect would increase the mean deprojected velocity at the outer edge of the disk to  $\sim 170 \text{ km s}^{-1}$ . If, on the

other hand, the shallowness of the dip between the peaks has nothing to do with turbulent broadening, no correction is needed. The most we can say is that the mean circular velocity at the outer edge of the disk lies somewhere in the range 150-170 km s<sup>-1</sup>.

The wavelengths of the centers of the fitted profiles are given in the last column of Table 4. Figure 10 plots the radial velocities of the line centers against the orbital phase calculated from the Goranskii (2011) orbital ephemeris (column 3 of Table 1). If the Br12 emission line comes from an accretion disk around the compact star, its radial velocity should be vary sinusoidally with a maximum approaching velocity near phase 0.25. The solid line in the figure is a sine curve fitted to the observed velocities by least squares. The measurements are sparse and poorly distributed in orbital phase, so the fitted values of the amplitude and mean velocity of the sine curve are not meaningful. The phase of the sine curve is, however, fairly well constrained. The phase of maximum approaching velocity occurs at  $\phi_{orb} = 0.31 \pm 0.04$ , which is consistent with the value expected for an accretion disk around the compact object.

## 5. Summary and Discussion

In summary, our most important results are:

- The precession phases of the jet differ from the phases predicted by the Eikenberry et al. (2001) ephemeris by  $\Delta\Psi_3 \approx -0.03$ . Because this small phase shift could have been caused by a combination of jet nodding and intrinsic phase jitter, we conclude only that the Eikenberry et al. (2001) ephemeris still predicts the jet redshift phase to  $|\Delta\Psi_3| \lesssim 0.03$ . This means that the clock underlying the phase of the jet precession has had a single, constant period for more than 37 years. We can place an upper limit on any secular changes to the period by attributing all

the observed phase shift to a slowly-changing precession period. The implied upper limit to the rate of change of the period is, then,  $|\dot{P}_{jet}| \lesssim 2|\Delta\Psi_3|/E^2 \approx 10^{-5}$ , where  $E = 83$  is the number of elapsed cycles, and the time scale for any period change is  $P_{jet}/|\dot{P}_{jet}| \gtrsim 40,000$  years. The superhumps in the light curves of the SU UMa subclass of cataclysmic variables are caused by precession of the accretion disks in these systems, although it is generally the precession of an elliptical disk lying flat in the plane of the orbit, not a tilted disk (Patterson 2001). For comparison, the rates of change of the periods of superhumps are generally greater than  $|\dot{P}_{hump}| \approx 2 \times 10^{-5}$ , but a few well-determined values of  $|\dot{P}_{hump}|$  are somewhat less than  $10^{-5}$  (Kato et al. 2009). The superhump periods of SU UMa stars are typically just a few hours, however, so for even the most stable of them  $P_{hump}/\dot{P}_{hump} \approx 30$  years.

- The multicomponent, variable, P-Cygni profile of the He I  $\lambda 2.0587 \mu\text{m}$  emission line is direct evidence for an inhomogeneous and variable wind outflow. The maximum observed wind speed is  $\sim 900 \text{ km s}^{-1}$ . These properties compare favorably with earlier measurements of the wind properties (Fabrika 2004; Medvedev et al. 2013), although we do not see the strong dependence of wind speed on disk inclination found by Fabrika (1997). The He II emission from the 12-7 and 10-7 transitions at  $\lambda 1.6898 \mu\text{m}$  and  $\lambda 2.1891 \mu\text{m}$  respectively also come from this wind. We agree with Medvedev et al. (2013) that the redshifted part of the He II wind emission is obscured, greatly obscured in the case of the  $\lambda 1.6898 \mu\text{m}$  line. Because of this obscuration and because the obscuration is variable, the profiles of the lines are distorted and the distortions vary with time (see also the discussion of He II emission lines in Goranskii (2011)).
- The broad, usually double-peaked, emission in the higher members of the Brackett series are produced in an accretion disk around the compact star. Three lines of

evidence lead to this conclusion. First, the observed line profiles generally agree with model profiles produced by accretion disks. We attribute the disagreements between the observed and model profiles on two of the observing dates to a rotational disturbance during eclipse and to obscuration by the optically-thick edge of the disk when the disk is edge-on, neither of which effects are included in the model. Second, the derived distribution of line flux across the disk is similar to the distribution of line flux across the surfaces of disks in cataclysmic variables and low-mass X-ray binaries. Third, the phase of the radial velocity curve of the Brackett lines agrees with the phase expected for an accretion disk around the compact star. Our conclusion is similar to that of Filippenko et al. (1988) who showed that the higher members of the Paschen lines could be modeled by emission from an accretion disk.

Our model differs from essentially every published model for the Balmer emission lines, especially the  $H\alpha$  line (Fabrika 2004). We attribute the difference to a difference in the physical processes producing the lines: Emission from the wind dominates the lower members of the Balmer series, drowning out emission from other sources. Wind emission is much weaker in the higher members of the Paschen series and Brackett series, allowing contributions from other components of the SS 433 system to dominate. Our model also disagrees with the interpretation of  $Br\gamma$  by Perez & Blundell (2009). In part this is due to our application of the model to the higher members of the Brackett series, but another factor is also at work. The observed  $Br12$  line profile that differed the most from our model was obtained on 2015 July 30, when the accretion disk was almost edge-on and the low-velocity line emission was strongly self absorbed. All of the spectrograms obtained by Perez & Blundell (2009) were obtained near this same disk orientation. They did not detect the accretion disk because much of it was hidden at that precession phase.

Our results place an important limit the mass of the compact object. We first review the uncertainties in previous measurements of the masses of the stars in SS 433, then calculate the new upper limit on the mass of the compact object. The direct way to determine the masses of stars in binaries is to measure the radial velocity curves of the two stars. The most recent determination of the masses of the stars in SS 433 based on radial velocities was by Kubota et al. (2010), who found  $1.9 M_{\odot} \leq M_X \leq 4.9 M_{\odot}$ . They also carefully analyzed the uncertainties in the masses derived this way. Because of heating, the radial velocity of the A-star can be measured during only half the orbit. Furthermore, considerable judgement must be exercised when choosing which of its absorption lines to measure and when estimating corrections to the measured velocities to account for the heating. The radial velocity of the compact star must be measured from the emission lines arising in gas thought to follow its motion, usually He II  $\lambda 4686 \text{ \AA}$  or C II  $\lambda 7231, 7236 \text{ \AA}$  (Fabrika & Bychkova 1990; Gies et al. 2002b). However, extensive observations of the radial velocity curves of soft X-ray transients and cataclysmic variables have shown that emission-line radial velocities yield unreliable masses, even when the systems are in unusually clean states, such as dwarf novae in quiescence and soft X-ray transients at minimum light (Warner 1995; Marsh 1998; Casares & Charles 2006). As noted by Goranskii (2011) and Medvedev et al. (2013) and confirmed by us, the He II line arises mostly in the disk wind, not from regions close to the compact star. The profiles of the line are complex, highly variable, and have distortions correlated with orbital phase, introducing considerable doubt that He II is a good proxy for the motion of the compact star.

Blundell et al. (2008) and Perez & Blundell (2009) decomposed the  $H\alpha$  and  $Br\gamma$  emission lines into sets of up to six Gaussian functions, and identified a pair of red- and blue-displaced Gaussians as emission from a circumbinary disk of gas in a circular Keplerian motion. They equated the velocities of the Gaussians with the orbital velocity, which yielded a lower limit on the mass enclosed by the circumbinary disk. After subtracting the

mass of the A-star, they derived a mass of  $\sim 16 M_{\odot}$  for the compact star and its accretion disk. Even if the decomposition of the line profiles into Gaussians were to have physical meaning, the enhanced gas flow in the plane of the orbit is observed to have a large radial outflow velocity (Crampton & Hutchings 1981; Fabrika 1997; Fabrika et al. 1997; Fabrika 2004). The gas does not follow a circular Keplerian orbit, compromising masses based on the assumption that it does.

Finally, as typified by the work of Goranskii (2011, 2013), it is possible to measure the mass of the compact star in SS 433 without resorting to radial velocity measurements. Brinkmann et al. (1989) assumed that the A-star exactly fills its Roche lobe and that the X-ray eclipse in SS 433 is an eclipse by the A star of a thin jet of X-rays near the compact star. Since the orbital inclination of SS 433 is known, they were able to derive a mass ratio  $q = M_X/M_A = 0.1496$ , where  $M_A$  is the mass of the A star. Using only its photometric properties and distance, Goranskii (2013) derived a mass for the A-star and, from the mass ratio, a mass for the compact star. The assumption that the surface of A-star is identical to the surface of its Roche lobe is insecure, though, especially since the A-star might be a tilted rotator as required by slaved disk models for the jet precession (van den Heuvel et al. 1980). The derivation of the A-star mass from its photometric properties is, furthermore, a multi-step process, each step prone to its own uncertainties.

While we cannot fully determine the mass of the compact star in SS 433, we can use the profiles of the Brackett lines to place an independent constraint on its mass. The separation of the two stars in SS 433 is given by  $a^3 = G(M_X + M_A)P_{orb}^2/4\pi^2$ . Previous measurements of the masses of the stars tend to fall into two distinct groups: one with total masses near  $30 M_{\odot}$  and one with total masses near  $15 M_{\odot}$  (Kubota et al. 2010; Goranskii 2011). For the  $30 M_{\odot}$  group, the separation of the two stars is  $\sim 5.1 \times 10^{12}$  cm; while for the  $15 M_{\odot}$  group, the separation is  $\sim 4.0 \times 10^{12}$  cm. If we assume that the tidal truncation

radius of an accretion disk around the compact object is about 25% of the separation of the stars (Frank, King, & Raine 1992), the maximum disk radius is  $1.0 - 1.3 \times 10^{12}$  cm.

If the disk is Keplerian, the radius of the outer edge of the disk is given by  $R_{max} = GM_X/V_{R_{max}}^2$ , which leads to the mass limit  $M_X \leq R_{max}V_{R_{max}}^2/G$ . All the various values one might adopt for  $R_{max}$  and  $V_{R_{max}}$  yield low upper limits to  $M_X$ , indicating a low total mass for SS 433. We will, therefore, restrict our discussion to the smaller radius for the disk,  $R_{max} = 1.0 \times 10^{12}$  cm. The most stringent constraint on the mass of the compact star comes from adopting the smallest measured value of the deprojected rotational velocity,  $V_{R_{max}} = 107$  km s<sup>-1</sup> as measured on 2015 June 11. This yields a mass limit of  $M_X \leq 0.86 M_\odot$ . A more realistic upper limit comes from adopting the mean deprojected rotational velocity,  $V_{R_{max}} = 148$  km s<sup>-1</sup>, which yields  $M_X \leq 1.6 M_\odot$ . The most relaxed upper limit comes from increasing the adopted  $V_{R_{max}}$  by another 15%, to  $V_{R_{max}} = 170$  km s<sup>-1</sup>, to account for the possible effects of turbulent broadening on the line profile. In this case the mass limit increases to  $M_X \leq 2.2 M_\odot$ . The only recent mass determinations that are consistent with these limits are that of Goranskii (2011), who found  $M_X = 1.45 \pm 0.20 M_\odot$ , and (barely) that of Kubota et al. (2010), who found  $1.9 M_\odot \leq M_X \leq 4.9 M_\odot$ . These limits place the mass of the compact star much below the range of measured black hole masses but within the range of measured neutron star masses (Ozel et al. 2012).

In closing we note that our results are based on data from just five nights of observations. It is encouraging that the new data are in accord with previously published data where comparison is possible, notably with the Paschen line profiles observed by Filippenko et al. (1988) and with the Br $\gamma$  line profiles observed by Perez & Blundell (2009), at least at those orbital phases where our data overlaps theirs. Nevertheless, the observational properties of SS 433 are complex and not easily disentangled. The mass limit

we have derive for the compact star in SS 433 should be viewed with some caution until it is tested against a larger set of data.

This work used the Immersion Grating Infrared Spectrograph (IGRINS) that was developed under a collaboration between the University of Texas at Austin and the Korea Astronomy and Space Science Institute (KASI) with the financial support of the US National Science Foundation under grant AST-1229522, of the University of Texas at Austin, and of the Korean GMT Project of KASI.

McDonald Observatory (IGRINS).

## REFERENCES

- Abell, G. O., & Margon, B. 1979, *Nature*, 279, 701
- Barnes, A. D., Casares, J., Charles, P. A., Clark, J. S., Cornelisse, R., Knigge, C., & Steeghs, D. 2006, *MNRAS*, 365, 296
- Bell, M. R., Roberts, D. H., & Wardle, J. F. C. 2011, *ApJ*, 736, 118
- Blundell, K. M., Mioduszewski, A. J., Muxlow, T. W. B., Podsiadlowski, P., & Rupen, M. P. 2001, *ApJ*, 562, L79
- Blundell, K. M., Bowler, M. G., & Schmidtobreick, L. 2008, *ApJ*, 678, L47
- Bowler, M. G. 2010, *A&A*, 516, A24
- Bowler, M. G. 2011, *A&A*, 534, A112
- Bowler, M. G. 2013, *A&A*, 556, A149
- Brinkmann, W., Kawai, N., & Matsuoka, M. 1989, *A&A*, 218, L13
- Brinkmann, W., Kotani, T., & Kawai, N. 2005, *A&A*, 431, 575
- Casares, J., & Charles, P. 2006, *Adv. Space Res.*, 38, 2731
- Cherepashchuk, A. 2002, *Space Sci. Rev.*, 102, 23
- Chojnowski, S. D., Whelan, D. G., Wisniewski, J. P., et al. 2015, *AJ*, 149, 7
- Clark, J. S., Barnes, A. D., & Charles, P. A. 2007, *MNRAS*, 380, 263
- Crampton, D., & Hutchings, J. B. 1981, *Vistas Astron.*, 25, 13
- Doolan, S., & Blunder, K. M. 2009, *ApJ*, 698, L23

- Eikenberry, S. S., Cameron, P. B., Fierce, B. W., Kull, D. M., Dror, D. H., & Houck, J. R. 2001, *ApJ*, 561, 1027
- Fabian, A. C., & Rees, M. J. 1979, *MNRAS*, 187, 13
- Fabrika, S. N. 1997, *Astrophys. Space Sci.*, 252, 439
- Fabrika, S. 2004, *Ap&SS*, 12, 1
- Fabrika, S. N., & Bychkova, L. V. 1990, *A&A*, 240, L5
- Fabrika, S. N., Goranskij, V. P., Yu, V. et al. 1997, *Bull. Spec. Astrophys. Obs.*, 43, 109
- Filippenko, A. V., Romani, R. W., Sargent, W. L. W., & Blandford, R. D. 1988, *AJ*, 96, 242
- Frank, J., King, A., & Raine, D. 1992, “Accretion Power in Astrophysics, Second Edition” (Cambridge: Cambridge University Press)
- Fuchs, Y., Koch-Miramond, L., & Abraham, P. 2002, *ASP Conf. Series*, 271, 369
- Geballe, T. R., Najarro, F., Figer, D. F., Schlegelmilch, B. W., & de La Fuente, D. 2011, *Nature*, 479, 200
- Gies, D. R., McSwain, M. V., Riddle, R. L., et al. 2002a, *ApJ*, 566, 1069
- Gies, D. R., Huang, W., & McSwain, M. V. 2002b, *ApJ*, 578, L67
- Goranskii, V. P. 2011, *Peremennye Zvezdy*, 31, 1
- Goranskii, V. P. 2013, *Cent. Eur. Astrophys. Bull.*, 37, 251
- Goranskii, V. P., Esipov, V. F., & Cherepashchuk, A. M. 1998, *Astron. Repts.*, 42, 336
- Greenstein, J. L., & Kraft, R. P. 1959, *ApJ*, 130, 99

- Hill wig, T. C., & Gies, D. R. 2008, ApJ, 676, L37
- Horne, K., & Saar, S. H. 1991, ApJ, 374, L55
- Johnston, H. M., Kulkarni, S. R., & Oke, J. B. 1989 ApJ, 345, 492
- Kato, T., Imada, A., Uemura, M., Nogami, D. et al. 2009 PASJ, 61, S395
- Katz, J. I., Anderson, S. F., Margon, B., & Grandi, S. A. 1982, ApJ, 260, 780
- Kim, H. 2011, ApJ, 739, 102
- Kotani, T., Kawai, N., Matsuoka, M., & Brinkmann, W. 1996, PASJ, 48, 619
- Kotani, T., Trustkin, A., Valiullin, R., Kinugasa, K., et al. 2006, ApJ, 637, 486
- Kraft, R. P. 1959, ApJ, 130, 110
- Kubota, K., Ueda, Y., Fabrika, S., Medvedev, A., Barsukova, E. A., Sholukhova, O., & Goranskij, V. P. 2010, ApJ, 709, 1374
- Lee, J.-J. 2015, <https://zenodo.org/record/18579/export/hx#.V6yWmxS0FOF>
- Liebert, J., Angel, J. R. P., Hege, E. K., et al. 1979, Nature, 279, 384
- Liu, J.-F., Bai, Y., Wang, S., Justham, S., et al. 2015 Nature, 528, 108
- Margon, B. 1984, ARA&A, 22, 507
- Margon, B., Ford, H. C., Katz, J. I., Kwitter, K. B., Ulrich, R. K., & Stone, R. P. S. 1979a, ApJ, 230, L41
- Marion, B., Ford, H. C., Grandi, S. A., & Stone, R. P. S. 1979b, ApJ, 233, L63

- Marsh, T. R. 1998, in ASP Conf. Ser. 137, Wild Stars in the Old West: Proc. 13th North American Workshop on Cataclysmic Variables and Related Objects, ed. S. Howell, E. Kuulkers, & C. Woodward (San Francisco: ASP), 236
- Marshall, H. L., Canizares, C. R., Hillwig, T., Mioduszewski, A., et al. 2013, ApJ, 775, 75
- McAlary, C. W., & McLaren, R. A. 1980, ApJ, 240, 853
- Medvedev, P. S., Fabrika, S. N., Vasiliev, V. V., Goranskij, V. P., & Barsukova, E. A. 2013, Astronomy Letters, 39, 826
- Milgrom, M. 1979a, A&A, 76, L3
- Milgrom, M. 1979b, A&A, 78, L9
- Mirabel, I. F., & Rodríguez, L. F. 1999, ARA&A, 37, 409
- Murden, P., Clark, D. H., & Martin, P. G. 1980, MNRAS, 193, 135
- Özel, F., Psaltis, D., Narayan, R., & Villarreal, S. 2012, ApJ, 757, 55
- Park, C., Jaffe, D. T., Yuk, I.-S., et al. 2014, Proc. SPIE, 9147, 91471D
- Patterson, J. 2001, PASP, 113, 736
- Perez, S., & Blundell, K. M. 2009, MNRAS, 397, 849
- Perez, S., & Blundell, K. M. 2010, MNRAS, 408, 2
- Roberts, D. H., Wardle, J. F. C., Lipnick, S. L., Selesnick, P. L., & Slutsky, S. 2008, ApJ, 676, 584
- Sawada, K., Matsuda, T., & Hachisu, I. 1986, MNRAS, 219, 75
- Schmidtobreick, L., & Blundell, K. 2006, Ap&SS, 304, 271

- Shapiro, P. R., Milgrom, M., & Rees, M. J. 1986, *ApJS*, 60, 393
- Shklovskii, I. S. 1981, *Sov. Aston.*, 25, 315
- Smak, J. 1981, *Acta Astronomica*, 31, 395
- Stover, R. J. 1981, *ApJ*, 248, 684
- Strohmayer, T., & Bildsten, L. 2006, in *Compact Stellar X-Ray Sources*, ed. W. H. G. Lewin & M. van der Klis (Cambridge: Cambridge Univ. Press), p. 113
- Thompson, R. I., Rieke, G. H., Tokunaga, A. T., & Lebofsky, M. J. 1979, *ApJ*, 234, L135
- van den Heuvel, E. P. J., Ostriker, J. P., & Petterson, J. A. 1980, *A&A*, 81, L7
- van der Klis, M. 2006, in *Compact Stellar X-Ray Sources*, ed. W. H. G. Lewin & M. van der Klis (Cambridge: Cambridge Univ. Press), p. 39
- Vermeulen, R. C., Murdin, P. G., van den Heuvel, E. P. J., Fabrika, S. N. et al. 1993, *A&A*, 270, 204
- Warner, B. 1995, *Cataclysmic Variable Stars* (Cambridge: Cambridge University Press)
- Welsh, W. F., Horne, K., & Gomer, R. 1998, *MNRAS*, 298, 285

Table 1. Times and Phases of the Observations

| Date (UT)   | Date (JD) <sup>a</sup> | $\phi_{orb}$ <sup>b</sup> | $\Psi_3$ <sup>c</sup> |
|-------------|------------------------|---------------------------|-----------------------|
| 2014 May 24 | 2456802.92728          | 0.198                     | 0.88                  |
| 2014 Nov 21 | 2456983.55008          | 0.004                     | 0.99                  |
| 2015 May 27 | 2457170.89553          | 0.325                     | 0.15                  |
| 2015 Jun 11 | 2457185.79650          | 0.464                     | 0.24                  |
| 2015 Jul 30 | 2457234.74350          | 0.206                     | 0.54                  |

<sup>a</sup>Julian Day at the midpoint of the exposure sequence.

<sup>b</sup>Orbital phase calculated from the ephemeris of Goranskii (2011).

<sup>c</sup>Jet precession phase calculated from the ephemeris of Eikenberry et al. (2001) but with the zero time translated so that  $\Psi_3 = 0$  corresponds to the maximum blueshift of the  $z_-$  jet. See Section 2 in the text.

Table 2. Emission Lines in the Spectrum of SS 433 in the  $H$  and  $K$  Bands

| Stationary Lines |                               |                                 | Jet Lines  |                   |                                 |
|------------------|-------------------------------|---------------------------------|------------|-------------------|---------------------------------|
| Species          | Transition                    | Wavelength<br>( $\mu\text{m}$ ) | Species    | Transition        | Wavelength<br>( $\mu\text{m}$ ) |
| Br $\gamma$      | 4-7                           | 2.1661                          | P $\alpha$ | 3-4               | 1.8756                          |
| Br8              | 4-8                           | 1.9451                          | P $\beta$  | 3-5               | 1.2822                          |
| Br10             | 4-10                          | 1.7367                          |            |                   |                                 |
| $\vdots$         | $\vdots$                      | $\vdots$                        | Br $\beta$ | 4-6               | 2.6259                          |
| Br25             | 4-25                          | 1.4971                          | $\vdots$   | $\vdots$          |                                 |
|                  |                               |                                 | Br11       | 4-11              | 1.6811                          |
| Pf19             | 5-19                          | 2.4490                          |            |                   |                                 |
| $\vdots$         | $\vdots$                      | $\vdots$                        | He I       | $3p^3P^0 - 4d^3D$ | 1.7007                          |
| Pf28             | 5-28                          | 2.3545                          | He I       | $3d^3D - 4f^3F^0$ | 1.8691                          |
|                  |                               |                                 | He I       | $3d^3D - 4p^3P^0$ | 1.9548                          |
| He I             | $3p^3P^0 - 4d^3D$             | 1.7007                          | He I       | $3p^3P^0 - 4s^3S$ | 2.1126                          |
| He I             | $3p^3P^0 - 4s^3S$             | 2.1126                          |            |                   |                                 |
| He I             | $2s^1S - 2p^1P^0$             | 2.0587                          | He I       | $3d^1D - 4p^1P^0$ | 1.8556                          |
|                  |                               |                                 | He I       | $3p^1P^0 - 4d^1D$ | 1.9089                          |
| He II            | 12-7                          | 1.6923                          | He I       | $2s^1S - 2p^1P^0$ | 2.0587                          |
| He II            | 10-7                          | 2.1891                          |            |                   |                                 |
| Mg II            | $5s^2S_{1/2} - 5p^2P_{3/2}^0$ | 2.1375                          |            |                   |                                 |

Table 2—Continued

| Stationary Lines |                               |                                 | Jet Lines |            |                                 |
|------------------|-------------------------------|---------------------------------|-----------|------------|---------------------------------|
| Species          | Transition                    | Wavelength<br>( $\mu\text{m}$ ) | Species   | Transition | Wavelength<br>( $\mu\text{m}$ ) |
| Mg II            | $5s^2S_{1/2} - 5p^2P_{1/2}^0$ | 2.1438                          |           |            |                                 |

Table 3. Observed Redshifts of the Jet Emission Lines

| Date (UT)   | $\Psi_3$ | $\Delta z_+$ | $\Delta z_-$ |
|-------------|----------|--------------|--------------|
| 2014 May 24 | 0.88     | 0.1510       | -0.0775      |
| 2014 Nov 21 | 0.99     | 0.1640       | -0.0882      |
| 2015 May 27 | 0.15     | 0.1200       | -0.0465      |
| 2015 Jun 11 | 0.24     | 0.0699       | ...          |
| 2015 Jul 30 | 0.54     | -0.0090      | 0.0760       |

Table 4. Fitted Parameters for the Disk Emission Line Model

| Date<br>(UT) | $R_{max}/R_{min}$ | $\alpha$ | $V_{turb}/V_{circ}$ | Disk<br>Inclination <sup>a</sup> | $V_{R_{max}}$ <sup>b</sup><br>(km s <sup>-1</sup> ) | Line Center<br>( $\mu\text{m}$ ) |
|--------------|-------------------|----------|---------------------|----------------------------------|---|----------------------------------|
| 2014 May 24  | 100               | 2.1      | 0.20                | 63°                              | 147   | 1.64135(05)                      |
| 2014 Nov 21  | 110               | 1.7      | 0.20                | 57°                              | 148   | 1.64190(10)                      |
| 2015 May 27  | 100               | 1.4      | 0.22                | 66°                              | 191   | 1.64120(05)                      |
| 2015 Jun 11  | 100               | 2.2      | 0.20                | 77°                              | 107   | 1.64155(10)                      |
| 2015 Jul 30  | 80                | 1.7      | 0.22                | 98°                              | ...   | 1.64142(05)                      |

<sup>a</sup>The disk is assumed to be perpendicular to the jet, whose inclination is determined from the jet precession ephemeris. At an inclination of 90° the disk is edge-on.

<sup>b</sup>Deprojected orbital velocity at the outer edge of the disk.

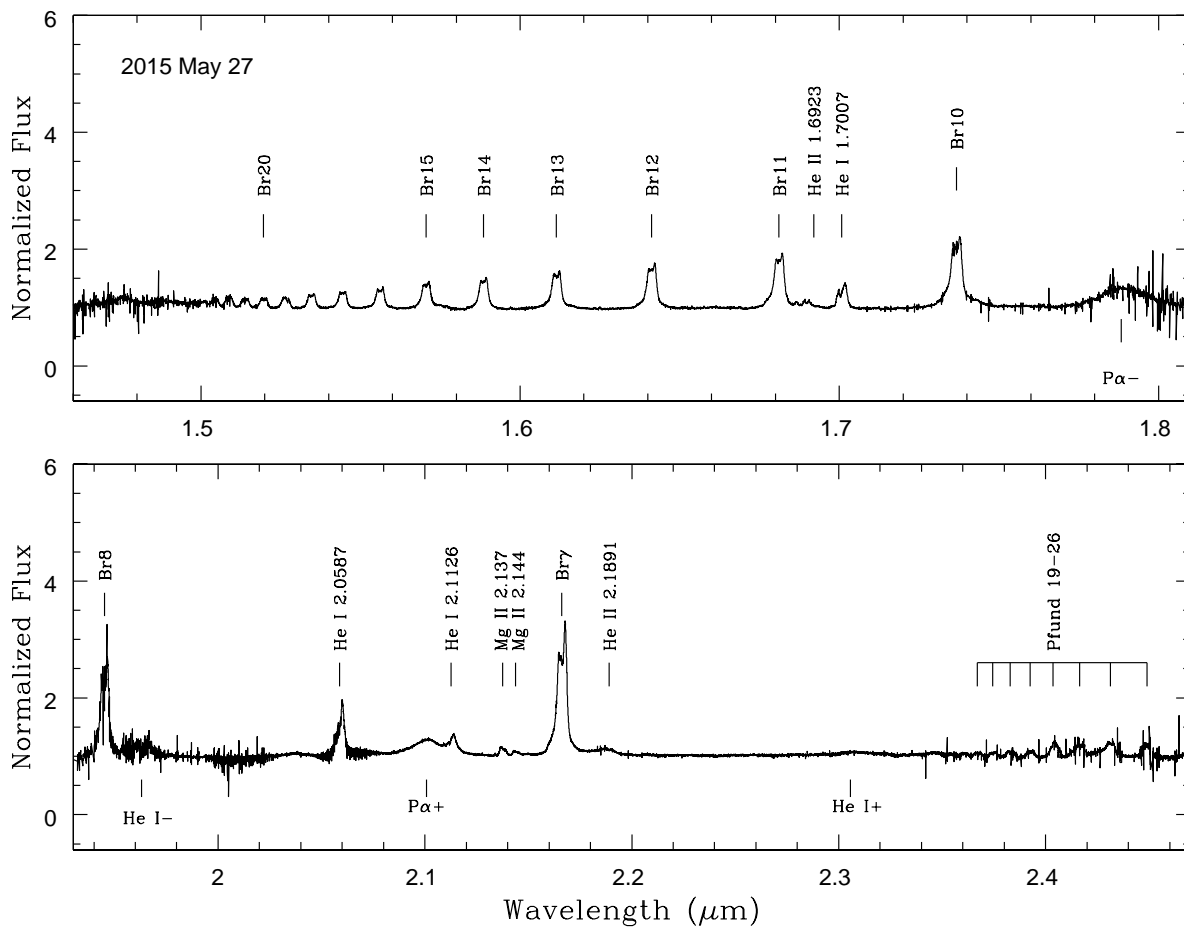


Fig. 1.— The spectrum of SS 433 obtained on 27 May 2015. The jet lines were unusually weak at that time, allowing the stationary lines to be identified without confusion. The stationary lines are marked and identified above the spectrum. The jet lines are marked and identified below the spectrum.

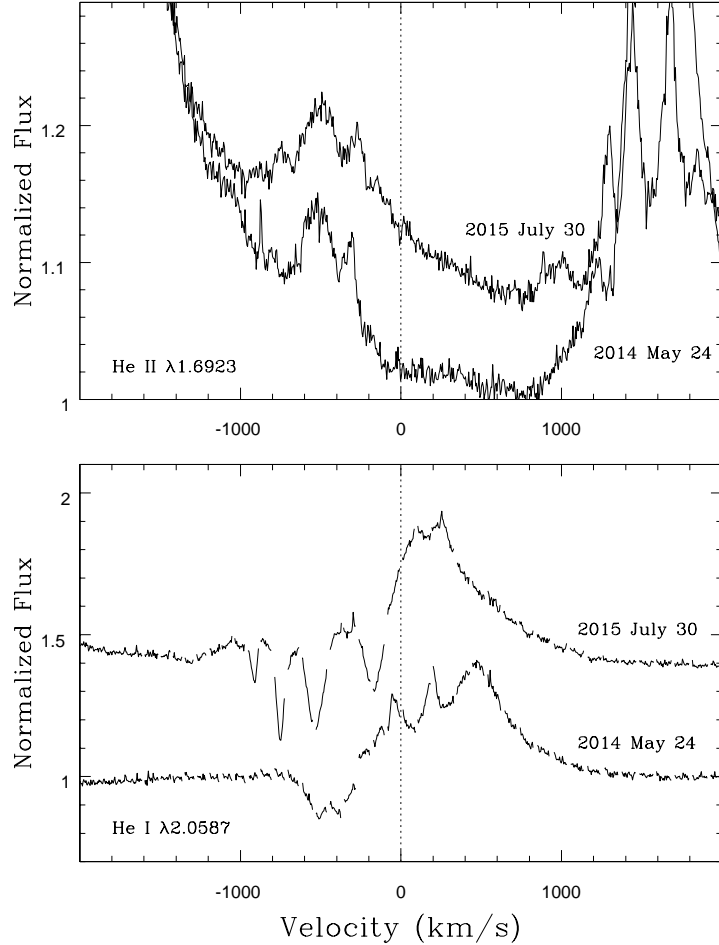


Fig. 2.— The bottom panel shows the profiles of the He I  $\lambda 2.0587$   $\mu\text{m}$  line on 2015 July 30 when the accretion disk was nearly edge on ( $i = 98^\circ$ ), and 2014 May 24 when the disk was most nearly face on ( $i = 63^\circ$ ). The telluric lines have been masked out in both spectrograms and the spectrum on 2015 July 30 has been shifted vertically for clarity. The wavelength scale has been converted to velocity shift from the rest wavelength of the line. The blue-shifted absorption features betray the presence of a complex and variable wind outflow. The top panel shows the profiles of the He II  $\lambda 1.6923$   $\mu\text{m}$  line on the same dates and, once again, the spectrum on 2015 July 30 has been shifted for clarity. This weak line lies on the steeply sloping red wing of the strong Br11 line. The He II line is shifted and broadened to roughly the same velocities as the wind features in the He I line, showing that it, too, arises in the disk wind.

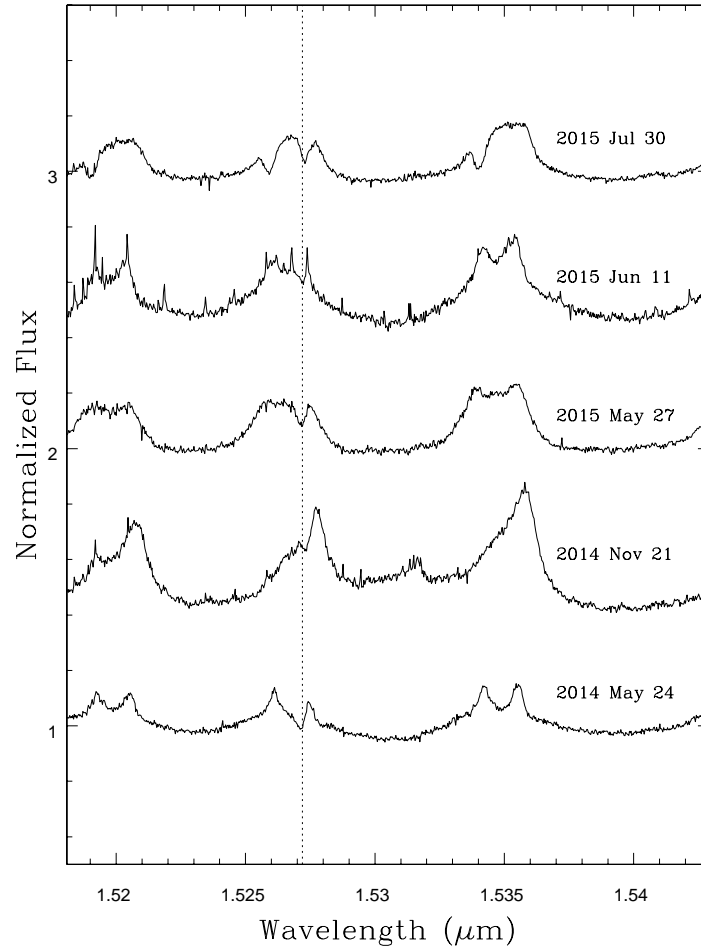


Fig. 3.— The Br18 (rightmost), Br19, and Br20 emission lines in all five spectrograms, labeled with the dates on which the data were obtained. The forest of narrow features present in all the spectrograms, but especially evident in the spectrogram obtained on 2015 June 11, are caused by incompletely removed terrestrial absorption lines. The profiles of all the Brackett lines are generally similar, as can be seen by comparing the profiles of the Br18 and Br20 lines. The broad absorption feature near  $1.5273 \mu\text{m}$  that distorts the profile of Br19 is a diffuse interstellar band.

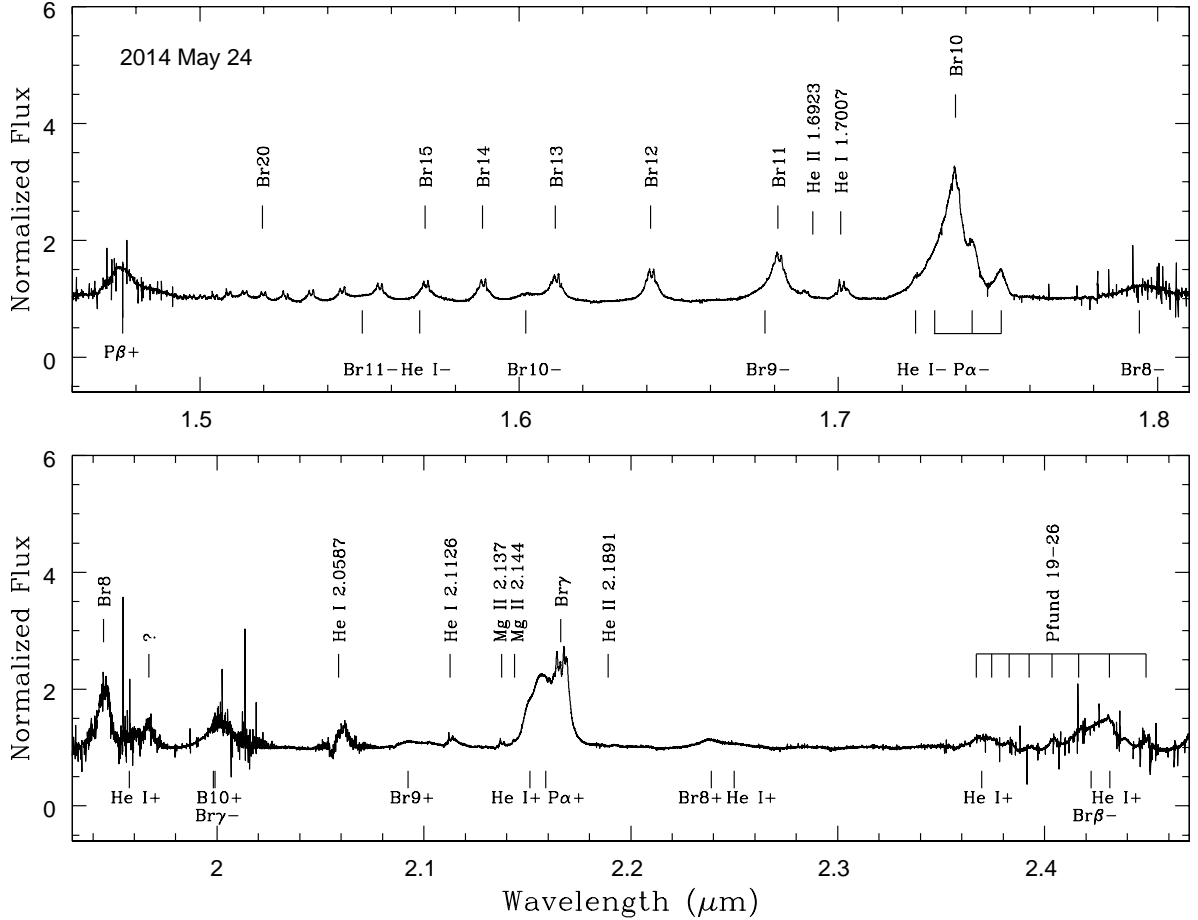


Fig. 4.— The spectrum of SS 433 obtained on 24 May 2014. The stationary lines are marked and identified above the spectrum, while the jet lines are marked and identified below the spectrum. The velocity shifts of the jet lines placed the  $P\alpha-$  and  $P\alpha+$  lines on top of the stationary Br10 and Br $\gamma$  lines respectively, greatly distorting the profiles of those stationary lines. We interpret the multi-peaked profile of the  $P\alpha-$  line sitting on top of Br10 as caused by “bullets” in the jet.

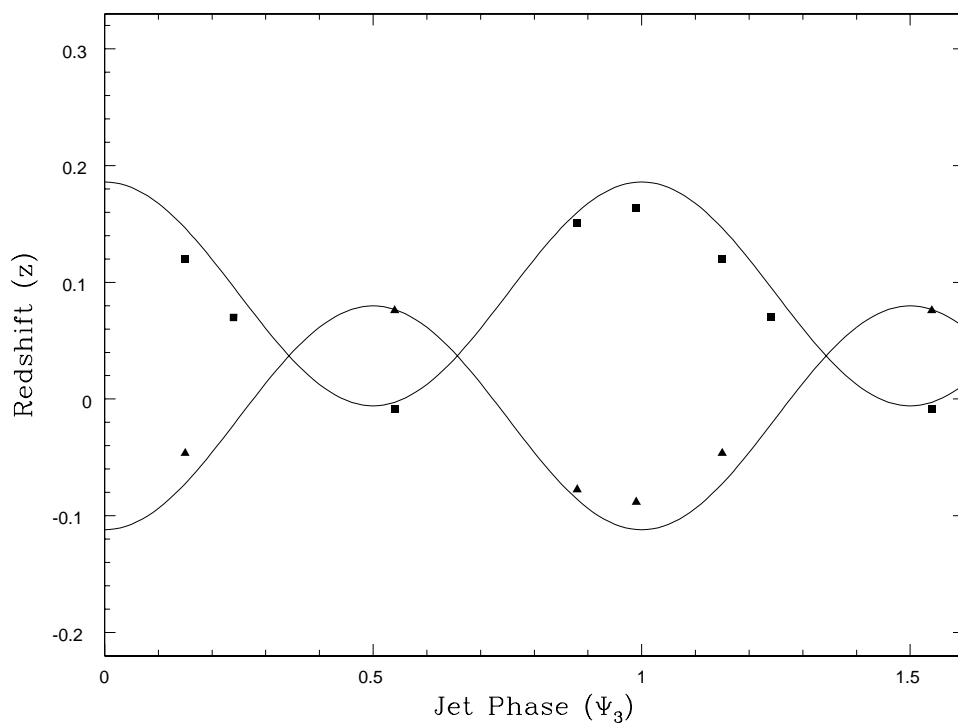


Fig. 5.— The filled squares and triangles are the measured redshifts of the jet lines in our data. At the scale of this plot the error bars are smaller than the symbols. The curves are the redshifts predicted by the Eikenberry et al. (2001) model for the jet reshifts. A shift of the predicted redshift curves by  $\Delta\Psi_3 \approx -0.03$  or about 5 days would bring the observed and predicted redshifts to the same phase.

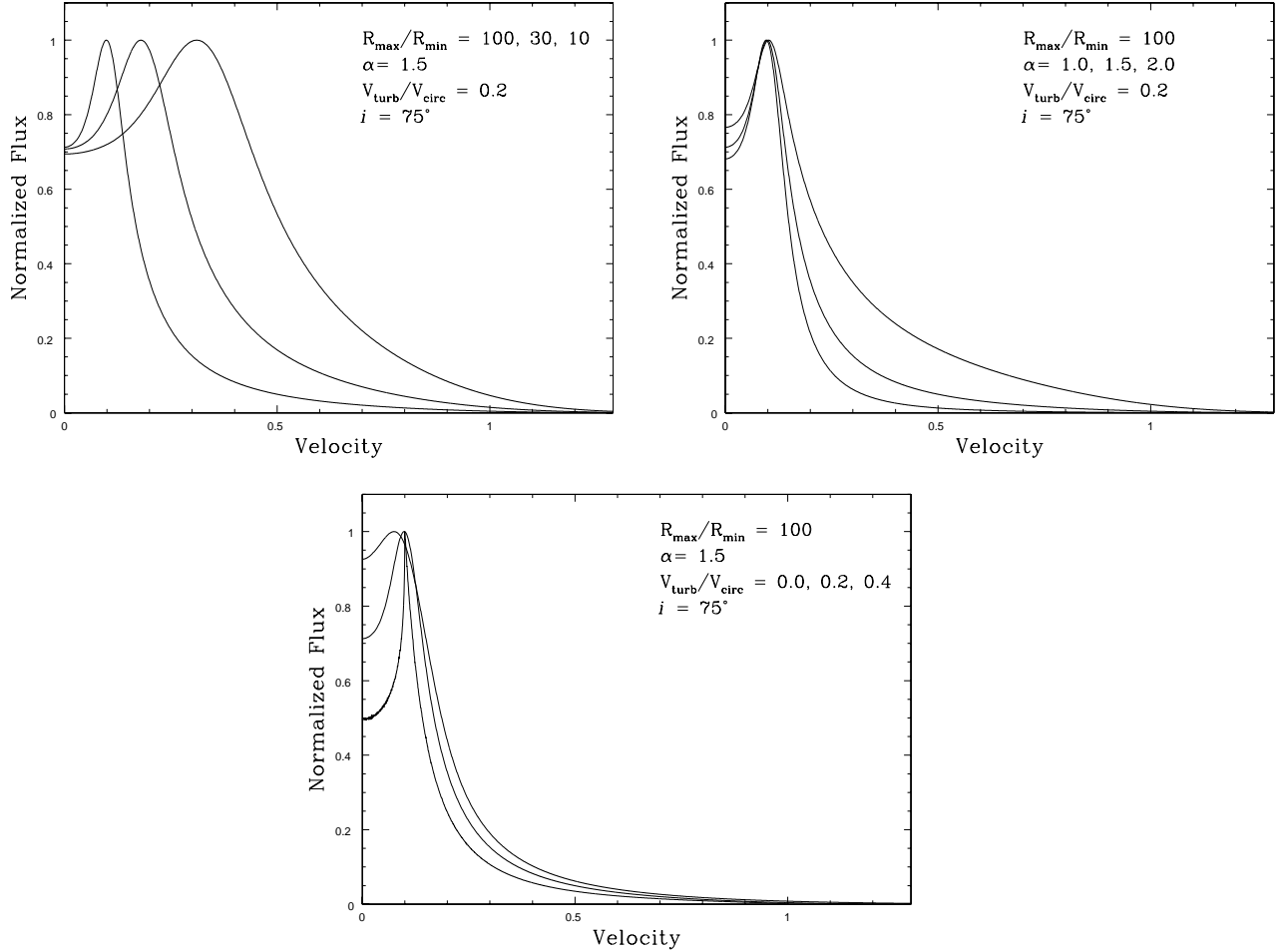


Fig. 6.— Model emission line profiles. The basic morphology of the profile – double-peaked with broad wings – is independent of the model parameters over their ranges of interest. The upper left panel shows the effect of varying the parameter  $R_{\max}/R_{\min}$ . The dominant effect is to increase the separation of the peaks relative to the total line width as  $R_{\max}/R_{\min}$  decreases. The upper right panel shows the effect of varying the parameter  $\alpha$ , where the line flux from the disk is given by the power law  $F \propto r^{-\alpha}$ . The dominant effect is to throw more flux into the line wings as  $\alpha$  decreases. The lower panel shows the effect of varying the turbulent velocity of the gas in the disk. The dominant effect of changing  $V_{\text{turb}}/V_{\text{circ}}$  is to decrease the depth of the minimum between the two peaks as the turbulent velocity increases.

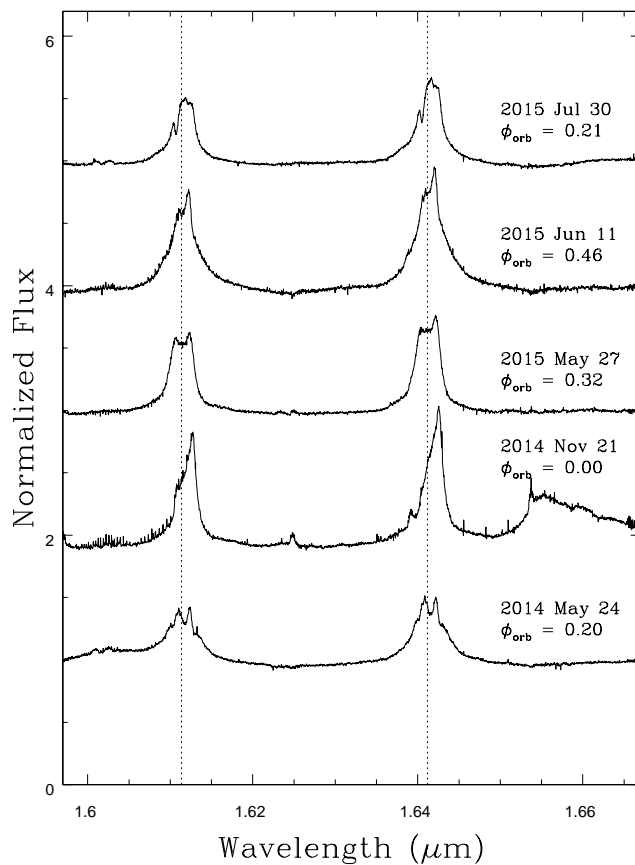


Fig. 7.— The Br12 and Br13 lines in all five spectrograms, labeled with the dates and the orbital phases at which the data were obtained. The forest of narrow features present in all the spectrograms, but especially evident in the spectrogram obtained on 2014 November 21, are caused by incompletely removed terrestrial absorption lines. Features near 1.625  $\mu\text{m}$  are artifacts introduced by inaccurate flat-fielding at the ends of orders. The broad feature at 1.655  $\mu\text{m}$  in the spectrum obtained on 2014 November 21 is the jet line Br9–.

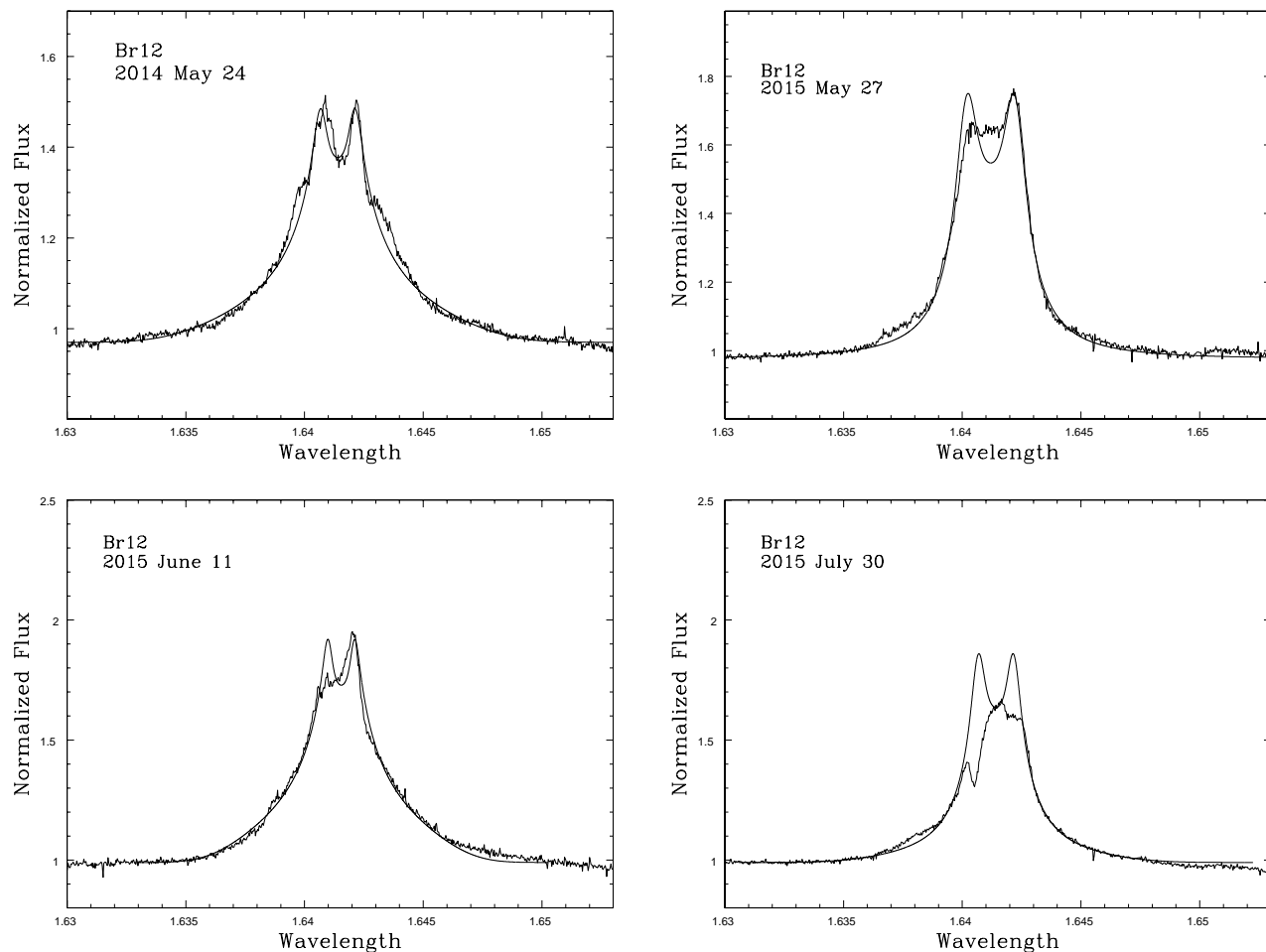


Fig. 8.— Fits of the accretion disk line profile model to the Br12 emission line on the dates labeled in the upper left corner of each panel. According to the Eikenberry et al. (2001) ephemeris, the inclinations of the jet to the line of sight were  $\theta = 63^\circ$  and  $66^\circ$  in the upper two panels, and  $\theta = 77^\circ$  and  $98^\circ$  in the lower two panels. If the accretion disk is perpendicular to the jet, the disk was viewed nearly edge-on in the lower right panel, perhaps explaining the missing horns of the line profile at that time.

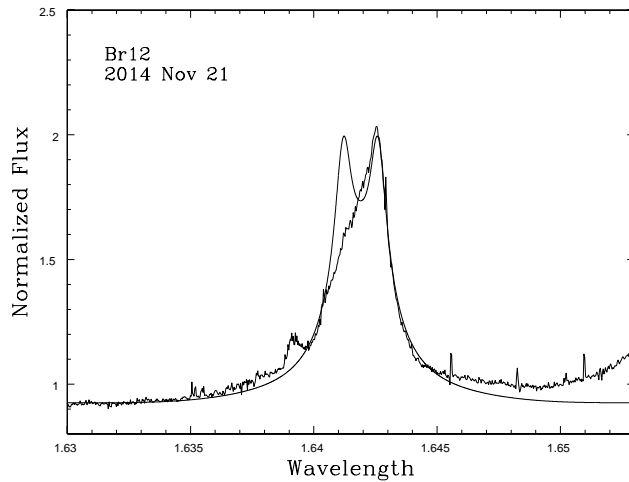


Fig. 9.— A fit of the accretion disk line profile model to the Br12 emission line on 2015 November 21. The rising flux on the right side of the spectrum is caused by the jet line Br9—. According to the Goranskii (2011) ephemeris, the orbital phase of SS 433 was  $\phi_{orb} = 0.00$  when the spectrogram was obtained. The profile of the Br12 line is similar to the profile of the Br $\gamma$  line at  $\phi_{orb} = 0.96$  shown Figure 1 in Perez & Blundell (2009). Although the sample is small, we suggest that the distortion of the line profile near and just before eclipse is repeatable. We interpret the distortion as being caused by a partial eclipse of the accretion disk.

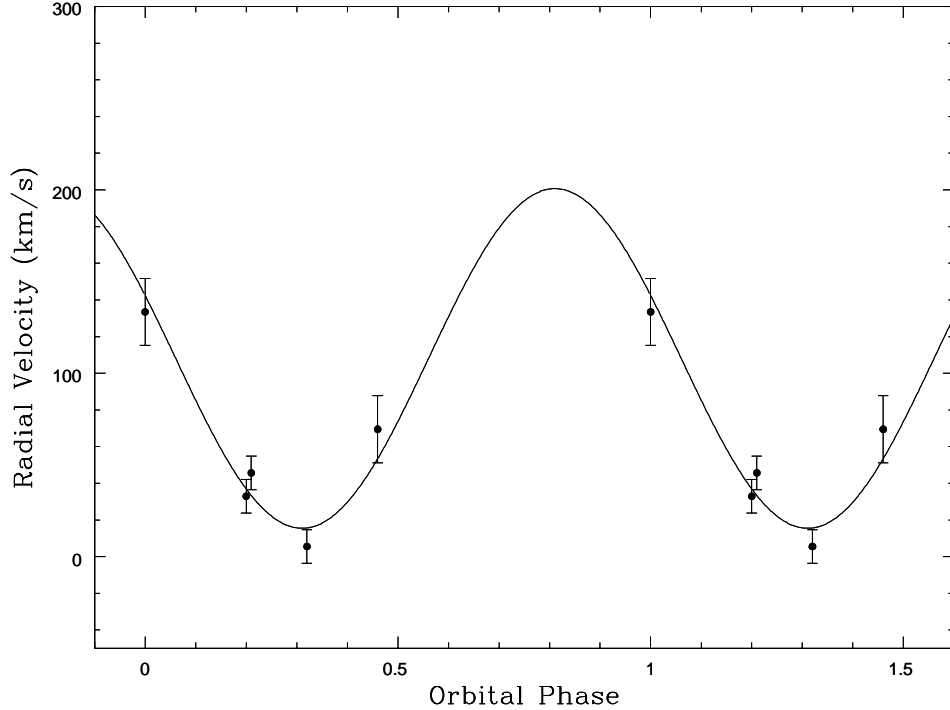


Fig. 10.— The data points are the radial velocities of the Br12 emission line plotted against the orbital phase calculated from the Goranskii (2011) orbital ephemeris. If the Br12 emission line comes from a symmetric accretion disk around the compact star, its radial velocity should vary sinusoidally with a maximum approaching velocity at phase 0.25. The solid line is a sine curve fitted to the data points. The measured velocities are sparse and poorly distributed in orbital phase, so the values of the amplitude and mean velocity are not meaningful. The phase of the sine curve is, however, fairly well constrained and is  $\phi_{orb} = 0.31 \pm 0.04$ .